



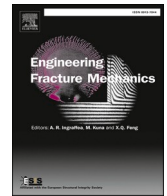
Analysis of thermal embrittlement of a low alloy steel weldment using fracture toughness and microstructural investigations

Downloaded from: <https://research.chalmers.se>, 2024-03-13 08:07 UTC

Citation for the original published paper (version of record):

Boasen, M., Lindgren, K., Öberg, M. et al (2022). Analysis of thermal embrittlement of a low alloy steel weldment using fracture toughness and microstructural investigations. *Engineering Fracture Mechanics*, 262. <http://dx.doi.org/10.1016/j.engfracmech.2022.108248>

N.B. When citing this work, cite the original published paper.



Analysis of thermal embrittlement of a low alloy steel weldment using fracture toughness and microstructural investigations

Magnus Boåsen^{a,*}, Kristina Lindgren^b, Martin Öberg^a, Mattias Thuvander^b, Jonas Faleskog^a, Pål Efsing^a

^a Solid Mechanics, Department of Engineering Mechanics, KTH Royal Institute of Technology, SE-100 44 Stockholm Sweden

^b Department of Physics, Chalmers University of Technology, SE-412 96 Göteborg, Sweden

ABSTRACT

A thermally aged low alloy steel weld metal is investigated in terms of its fracture toughness and microstructural evolution and compared to a reference. The main purpose of the study is to investigate the effects of embrittlement due to thermal ageing on the brittle fracture toughness, and its effects on the influence of loss of crack tip constraint. The comparison of the investigated materials has been made at temperatures that give the same median fracture toughness of the high constraint specimens, ensuring comparability of the low constraint specimens. Ageing appears to enable brittle fracture initiation from grain boundaries besides initiation from second phase particles, making the fracture toughness distribution bimodal. Consequently, this appears to reduce the fracture toughness of the low constraint specimens of the aged material as compared to the reference material. The microstructure is investigated at the nano scale using atom probe tomography where nanometer sized Ni-Mn-rich clusters, precipitated during ageing, are found primarily situated on dislocation lines.

1. Introduction

When assessing degradation due to ageing in low alloy steels used as structural materials in pressure vessel components both base and weld metals must be considered, as for example in reactor pressure vessels in nuclear power plants. In this type of materials in nuclear applications, ageing mainly occurs by neutron irradiation and thermal ageing, and generally manifests itself as a hardening effect and an increase in the ductile-to-brittle transition temperature, or in another word, *embrittlement*. In pressurized water reactors (PWRs), the pressurizer regulates the system pressure and thereby the temperature within the primary loop such that the water is kept from boiling. Following the replacement of the pressurizer in Ringhals unit 4 (R4) in 2011, material extraction was carried out in order to study potential ageing effects on the materials after 28 years of operation. Initial investigations of two of the weldments from the pressurizer material displayed a noteworthy increase in the transition temperature $\Delta T_{41J} = \{78 \text{ and } 71\}^\circ\text{C}$ and an increase of the yield strength $\Delta R_{p02} = \{128 \text{ and } 59\} \text{ MPa}$, displaying a clear indication of embrittlement due to thermal ageing at the operating temperature of 345°C (no irradiation present in the pressurizer).

Embrittlement is a key aspect in the structural integrity ageing assessment of any structure. Therefore, understanding the changes in the fracture toughness and all its features for a material that undergoes embrittlement is necessary. The cleavage fracture toughness of ferritic steels is strongly dependent on temperature, size and crack tip constraint. Generally, it can be stated that higher temperature endorses a more ductile behavior, larger specimens or components will be more brittle, and high constraint will produce a lower fracture toughness than low constraint. To our knowledge, no studies have been published concerning the constraint effect on fracture toughness after the material has undergone embrittlement and how this relates to the behavior of a reference material.

* Corresponding author at: KTH Solid Mechanics, Teknikringen 8D, SE-100 44 Stockholm Sweden.

E-mail address: boasen@kth.se (M. Boåsen).

The prevailing explanation of embrittlement due to thermal ageing of low alloy steels in nuclear applications is impurity segregation towards prior austenite grain boundaries, e.g. phosphorus, commonly referred to as grain boundary embrittlement. Studies of thermal ageing include a wide spectra of base and weld metals from reactor types such as the VVER-1000 [1–4], as well as the western PWRs featuring the typical steels A508 and A533 or its equivalents [5–11]. All studies referenced here, report on intergranular fracture due to impurity segregation caused by thermal ageing.

In the extensive review of intergranular failure in steels by Briant and Banerji [12], it is noted that some distinguishable phenomena appear to be related to intergranular failure. One being that segregation of elements from groups IV–VI in the periodic table appears to yield the most potent grain boundary embrittlement, which is also mentioned by McMahon [13]. These groups include elements such as Si, Sn, P and S, which are not uncommon impurities or alloying elements in the steels of interest. Another is that a grain size effect appears to emerge where microstructures with larger grains yields more intergranular fracture than for the case of smaller grains. The authors of [12] speculate that this could be due to a dilution of the impurity elements due to the difference in grain boundary area in relation to grain volume, for the case of smaller grains. This implies that a microstructure with smaller grains would result in a larger degree of dilution of impurities across the grain boundaries and thus less embrittlement, than in a microstructure with larger grains *ceteris paribus*. Another notable phenomenon is the effect of co-segregation of elements such as Ni and Mn, which is indicated to yield a faster and more potent embrittlement [12,14,15]. In a study by Banerji et al. [16] concerning the effects of impurities and hydrogen on intergranular fracture in a commercial steel, several heats were tempered at different temperatures in the range 50–625 °C and then subjected to Charpy impact testing at room temperature. One of the findings in the study was that the largest decrease of the absorbed energy appeared after tempering at ~ 350 °C with resulting intergranular facets covering the fracture surfaces. Also, a similar grain size dependency as reported in [12] could be observed, i.e. larger grains yielding more embrittlement at the same conditions.

Grain boundary embrittlement as a result of thermal ageing will act as a non-hardening embrittlement since it, in general, does not impede dislocation motion, and gives rise to a fracture morphology with a large incidence of grain boundary facets. It also appears to have several commonalities with the phenomenon called reversible temper embrittlement [12,17]. The hardening effect that is typically observed in irradiated low alloy steels comes to a large extent from the formation of solute clusters, but also clusters of either interstitials or vacancies, during irradiation. The hardening effect is due to that the clusters act as obstacles to dislocation motion, thereby increasing the resistance to plastic flow. In the case of the weldments of most of the Swedish reactor pressure vessels, the irradiation induced solute clusters consist mainly of Mn, Ni, Si and Cu [18–20]. The formation of similar clusters in a thermally aged weld metal has also been observed by Lindgren et al. [21]. In that study, solute clusters are noted to have been formed preferentially on dislocations as observed by atom probe tomography (APT) and is related to the thermally ageing induced hardening of the weld metal. It should be noted that the weldment investigated in this study and the one investigated by Lindgren et al. were extracted from the same pressurizer but from different welds. However, both welds were manufactured with the same welding specifications. In other atom probe studies of thermally aged low alloy steels [22–25], solute clusters of similar composition as the ones in [21] were found, however these findings were not connected to any changes in mechanical properties.

The weld investigated in this study is a multi-layer weldment, which signifies that the weld is built up by several layers of weld beads. This gives rise to a complex microstructure where three distinct grain zones will emerge. These zones are:

- I. the as-welded zone, consisting of elongated dendritic grains,
- II. the once reheated zone, consisting of small equiaxed grains, and
- III. the multiple reheated zone, also consisting of small equiaxed grains.

This will give rise to variations in several properties such as local chemistry, fracture toughness and other mechanical properties. An interesting study of the fracture toughness of multi-layer weldments was made by Viehrig et al. [26].

The main purpose of the testing conducted in this paper is to investigate the effects of thermal ageing on the brittle fracture toughness, and its effects on the influence of loss of constraint. Since ageing also may lead to weakened grain boundaries, it is also of interest to investigate to what extent this may contribute to the embrittlement. Thus, the core of this paper is an investigation of the fracture toughness of an in-service thermally aged weld metal from a Swedish nuclear power plant. This is compared to a reference material from a replaced reactor pressure vessel head, which has been in operation at a lower temperature than the pressurizer and where the effects of ageing therefore are considered minor. The study presents the results from an extensive experimental program where effects of ageing on the constraint sensitivity has been a focal point. Moreover, results from ductile fracture toughness testing, and tensile as well as hardness testing are presented along with an examination of the materials microstructure on the nano scale.

The outline of the paper is as follows: Section 2 presents the materials used in this study in terms of chemical composition, as-manufactured mechanical properties, along with the experimental set-up used. Section 3 presents the outcome of the experimental program including fractography and results from APT.

2. Materials and experiments

2.1. Materials

The thermally aged material investigated in this study has been extracted from the decommissioned and replaced pressurizer of the Ringhals unit 4 reactor. The pressurizer was manufactured by Uddcomb from plates of low alloy steel of the type A-533 Gr B Cl. 1 The weld metal comes from the circumferential weldment connecting the lower head to the first cylindrical structure of the pressurizer. The studied weld was manufactured using submerged-arc welding employing a weld wire with a low Cu – high Mn-Ni content,

Table 1

Chemical composition of the investigated weld metals from the manufacturing documentation.

Wt. %	C	Si	P	S	V	Cr	Mn	Co	Ni	Cu	Mo	Sn	Fe
R4PRZ	0.082	0.20	0.013	0.006	0.004	0.14	1.62	0.008	1.61	0.06	0.45	0.005	Bal.
R3RPVH	0.08	0.22	0.008	0.006	0.000	0.03	1.66	0.019	1.57	0.07	0.49	0.002	Bal.

Table 2

Check-in mechanical properties of the investigated weld metals.

	R_{p02}/MPa	T_{411}/C
R4PRZ	579	−53
R3RPVH	575	−59

characteristic for all of the nuclear pressure vessels manufactured by Uddcomb. The measured chemical composition of the welding wire and flux combination can be found in Table 1. A post weld heat treatment was conducted for residual stress relief at 620 °C as part of the fabrication procedure. The pressurizer was in operation from 1983 to 2011, gathering a total of 215 000 h at an operating temperature of 345 °C. The pressurizer was well insulated during its operation and consequently the temperature gradient through the thickness can be considered negligible. The results from check-in mechanical testing of the weld metal can be found in Table 2. The material from the pressurizer will henceforth be denoted as R4PRZ.

A reference material extracted from the replaced reactor pressure vessel head of Ringhals unit 3 was also included in the testing program for comparison purposes. This material was used in the investigation since there was no archive material available for the pressurizer. The reference material was chosen to have as similar Cu-Mn-Ni-Si content and check-in mechanical properties as the thermally aged weldment from the pressurizer as possible from the available material. The reactor pressure vessel head was manufactured from forgings of A-508Cl. 2 by Uddcomb and was welded using the same manufacturing specifications as the R4PRZ. The measured chemical composition of the reference material can be found in Table 1, and the check-in mechanical properties in Table 2. The reference material was in operation between 1981 and 2005 accumulating 176 000 h at 310–315 °C. Preliminary testing (not presented here) showed that the effects of thermal ageing at this operating temperature were minor in comparison to those of the pressurizer. The reference material will be denoted as R3RPVH throughout this paper.

2.2. Fracture testing

The fracture toughness testing in the investigation of the constraint effect utilizes SEN(B)-specimens with the same overall dimensions but with different crack depth, deep for a state of high constraint and shallow for low constraint, for an illustration see Fig. 1. Also included in the study is a small, deeply cracked SEN(B)-specimen, serving as a reference. All specimens were extracted as T-S oriented with dimensions $W = \{30 \text{ and } 14\} \text{ mm}$, $B = \{15 \text{ and } 7\} \text{ mm}$, $a/W = \{0.5 \text{ and } 0.1\}$, and were manufactured such that the weld was centered in the specimen with base metal on each side. All specimens within the same dataset have been taken from the same depth of the weld metal with the purpose to have as similar weld microstructure in each specimen as possible. Thus, all the specimens with the same crack depth will have comparable microstructures. The specimens were placed in the weld to avoid the region close to the surface and the root of the weld. All specimens for investigation of the brittle fracture toughness were manufactured without side-grooves.

The testing for the brittle fracture toughness was conducted in accordance with ASTM E1921 [27], with the exception that the standard does not cover testing of specimens containing shallow cracks. The cracks were created using fatigue pre-cracking at room temperature according to the recommendations in E1921, which resulted in straight crack fronts in all specimens. When pre-cracking the shallow specimens, the crack length was estimated using a strain measurement technique. Testing was carried out in a computer-controlled cooling chamber utilizing liquid nitrogen to cool the specimen. The fracture toughness testing was carried out in displacement control with a loading rate corresponding to $1 \text{ MPa}\sqrt{\text{m/s}}$ during the initial elastic region of the test. The fracture toughness was evaluated from the load line displacement. The J -integral at failure was calculated from the load line displacement where the plastic η -factor valid for shallow cracks in SEN(B)-specimens was taken from Faleskog et al. [28].

The brittle fracture toughness results were interpreted by means of the master curve standard ASTM E1921 [27]. The ductile-to-brittle reference temperature T_0 was evaluated according to that standard. The master curve concept is based on a probabilistic weakest link model for brittle cleavage fracture assuming small-scale yielding conditions and self-similar crack tip fields [29]. The probability of failure at K_{Jc} is expressed by

$$P_f = 1 - \exp\left(-\frac{B}{B_0} \left[\frac{K_{Jc} - K_{min}}{K_0 - K_{min}}\right]^4\right), \quad (1)$$

where B is the thickness of the specimen (or crack front width), B_0 is a reference thickness which is set to $1 \text{ T} = 25.4 \text{ mm}$, K_{min} is a threshold fracture toughness, and $K_0 = K_0(T)$ is a temperature dependent reference fracture toughness that is referenced to $10 \text{ MPa}\sqrt{\text{m}}$ for a 1 T specimen at T_0 . More specifically, K_0 is well described by

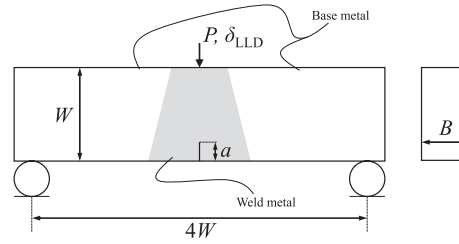


Fig. 1. Schematic illustration of a SEN(B)-specimen used in the experiments.

$$K_0 = 31 + 77 \exp(0.019[T - T_0]) \text{ MPa}\sqrt{\text{m}}. \quad (2)$$

For the master curve to give a good description of a materials brittle cleavage fracture toughness, the material itself needs to be homogeneous. In the case of a large degree of scatter due to material inhomogeneity, ASTM E1921 supplies additional methodology of T_0 -evaluation so that a conservative estimate of the fracture toughness can be ensured. One example of such a method is the SINTAP-methodology [30], which now has been included in E1921, where an additional safety factor is included in the evaluation of T_0 . Such methods may be needed in the evaluation of the fracture toughness of weld metals, where the scatter may be larger than that of more microstructurally homogeneous base metals. Another example is the case where the material displays a bimodal toughness distribution, where the bimodal master curve [31] can be utilized, which is expressed as

$$P_f = 1 - p_a \exp\left(-\frac{B}{B_0} \left[\frac{K_{Jc} - K_{\min}}{K_0^A(T_0^A) - K_{\min}}\right]^4\right) - (1 - p_a) \exp\left(-\frac{B}{B_0} \left[\frac{K_{Jc} - K_{\min}}{K_0^B(T_0^B) - K_{\min}}\right]^4\right). \quad (3)$$

The bimodal master curve requires three parameters that needs to be estimated, where T_0^A and T_0^B correspond to the reference temperature for each mechanism (mode in the distribution), respectively, and p_a is a probability scaling parameter that defines the contribution of each mechanism.

As the original master curve model is based on self-similar crack tip fields (small-scale yielding, high constraint), it is not capable of handling the effect of loss of constraint. In order to incorporate the effect of constraint, an empirical correction of T_0 by the T -stress is proposed by Wallin [32,33], as

$$T_0 = T_0^{\text{high constraint}} + \Delta T_0^{\text{constraint}}, \text{ where } \Delta T_0^{\text{constraint}} = A \frac{\Delta T_{\text{stress}}}{\sigma_y}. \quad (4)$$

Here, the difference in T -stress at the limit load between the predicted geometry and the geometry used to determine $T_0^{\text{high constraint}}$ should be used, where $T_0^{\text{high constraint}}$ normally is referred to as T_0 , as the standard test method prescribes the use of deeply cracked specimens that produce a state of high constraint. In (4), the factor A is a yield strength dependent parameter that is empirically found to be approximately $\sigma_y/10 \text{ MPa/K}$ [32] for $\sigma_y > 600 \text{ MPa}$ and constant equal to 40°C [33] when σ_y is below 600 MPa . It should be noted that the constraint correction of the master curve is still only partially developed for more complex geometries [34].

As the main purpose of this study is to investigate the sensitivity of the constraint effect on the fracture toughness of the thermally aged weld metal from the pressurizer and compare the results with the reference material available, a well-grounded approach is needed. An objective way to compare the constraint sensitivity of two materials is to choose the testing temperatures such that the median of the high constraint fracture toughness coincides. The next step is to conduct low constraint testing at the same temperatures, elucidating potential differences in the constraint effect on the fracture toughness between the two materials.

The testing was therefore conducted in the following steps:

- i. Initial test series according to ASTM E1921 to find the reference temperature T_0 for the two materials
- ii. use T_0 to determine temperatures where the high constraint fracture toughness will be the same for the two materials
- iii. conduct remaining test series at the chosen temperature, high and low constraint as well as small specimens.

From the test results in step i, T_0 was evaluated to determine the testing temperatures to be used in step iii. The testing temperatures that would yield the same high constraint brittle fracture toughness was chosen to be -50°C for R4PRZ and -90°C for R3RPVH. Both materials were tested in series of 12 specimens in step iii.

Alongside the tests for the brittle fracture toughness, tests for the ductile fracture toughness were also conducted. These were carried out at a temperature of 75°C to avoid brittle fracture altogether, i.e. clearly being on the upper shelf. The testing was performed with SEN(B)-specimens with side-grooves to promote uniform growth across the thickness of the specimens. The specimens for the ductile testing were extracted from the T-S orientation with dimensions $W = 30 \text{ mm}$, $B = 15 \text{ mm}$, $B_N = 12 \text{ mm}$, and $a/W = 0.5$. The testing was conducted in accordance with ASTM E1820 [35]. The J -integral was calculated from the crack mouth opening displacement (CMOD).

2.3. Tensile and hardness testing

Uniaxial tensile testing was carried out on round bar specimens of both the weld and the base metal. In addition, hardness testing was performed on the weld metal, before and after heat treatments at 430 °C and 600 °C, respectively. Note that different samples were used for the different temperatures. The hardness tests were performed to investigate the recovery of the ageing induced hardening during heat treatments. Hardness testing according to Vickers with an indentation load of 10 kgf was chosen as the test method. The specimens used were manufactured into blocks measuring 15 mm × 8 mm × 4 mm. An initial grid of indents was made to map out the initial hardness of the two materials, R4PRZ and R3RPVH, where the samples displayed a slight variation of hardness across the surface intended for measurement, as a result of the varying microstructure inherent to the weld. Hardness was also measured across and along the centerline of the weld in both materials.

2.4. Atom probe tomography

The nanostructure of the material has been investigated by APT, which was performed in a LEAP 3000X HR from Imago Scientific Instruments. From the results of the study in [21], it was expected that unevenly distributed Ni-Mn-Cu-Si rich clusters would be found. Due to this, large volumes, for APT, of material were analysed, and thus laser pulsing was used in addition to voltage pulsed analysis. However, laser pulsing affects the Si position due to surface diffusion [36] and thus both pulsing modes were used. For voltage pulsed analysis, a temperature of 50 K and pulse fraction of 20 % was used. For laser pulsed analysis, the temperature was 30 K and the laser energy 0.3 nJ. In both cases the laser pulse frequency was 200 kHz. The sample preparation was done using a standard two-step electropolishing method [37], finishing with millisecond pulsing to get rid of surface contamination. The reconstructions were made in the IVAS 3.6 software, using reconstruction parameters k between 4.0 and 5.3, and evaporation field of 33 V/nm in the case of voltage pulsed analysis and 23 V/nm for laser pulsed analysis. The image compression factor was set to 1.65 for all reconstructions.

The cluster analysis was performed using the maximum separation method (MSM) [38,39], a method that requires a careful choice of parameters in order to get relevant and comparable results [40,41]. Cluster parameters were chosen by comparing the data set to a randomised version and aiming to avoid defining random fluctuations in composition as clusters. Solute elements were chosen to be Cu, Ni, and Mn. The maximum solute atom distance in order for two atoms to be considered being in a cluster, d_{\max} , was set to 0.45 nm, and the smallest number of solute atoms defining a cluster, N_{\min} , was chosen to 20. Cluster sizes were determined by calculating the number of solute atoms in the clusters, assuming α -Fe body centred cubic structure and a detection efficiency of the LEAP of 37 %. The amount of Fe in the cluster is uncertain, since local magnification effects focus Fe atoms into the clusters during field evaporation [42,43]. Thus, the around 50 % Fe detected in clusters in these APT reconstructions is probably considerably lower in the actual material. Here, Fe was excluded from the clusters when calculating the size. This might give a slight underestimation if there is any Fe in the clusters. Cluster compositions were determined using MSM as well. For the number density, clusters on the edge of the analysis were identified and counted as half a cluster. It should be noted that the terms precipitate and cluster is used interchangeably in this paper, as the characterisation method (APT) does not give useful crystallographic information of the clusters.

3. Experimental results

3.1. Fracture toughness tests

In the evaluation of the reference temperature T_0 , it was observed that the two materials behaved differently, which was due to the degree of inhomogeneity. The thermally aged R4PRZ displays a larger degree of inhomogeneity and has therefore been evaluated with

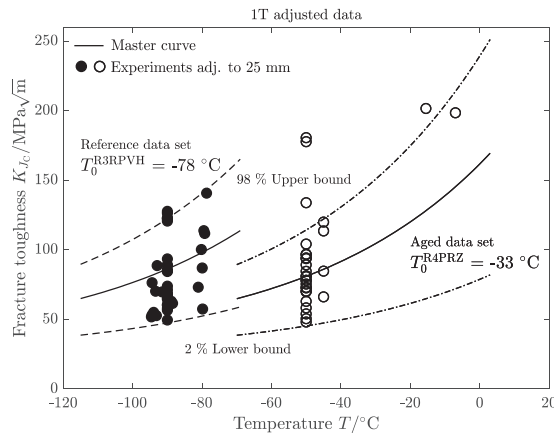


Fig. 2. Fracture toughness of individual specimens belonging to both R3RPVH and R4PRZ against testing temperature, and the predicted temperature dependence from the master curve model. Note that fracture toughness data for all deeply cracked specimens are presented in this figure.

the more conservative SINTAP-evaluation than that of the reference material R3RPVH, which was evaluated according to the normal procedure of E1921. The fracture toughness of deeply cracked specimens of both materials are shown as a function of testing temperature in Fig. 2 together with the master curve predictions based on the respective material's T_0 . It is clear that the thermally aged R4PRZ is more brittle than R3RPVH, with a difference in T_0 , $\Delta T_0 = 45$ °C. Estimating the T_{41J} from the T_0 of R3RPVH by the empirical relation supplied in E1921 ($T_{41J} = T_0 + 24$ °C) yields $T_{41J} = -54$ °C, which agrees well with the check-in values for T_{41J} listed in Table 2, giving justification to using R3RPVH as a (fracture toughness) reference to R4PRZ.

By looking at the ranked probability of the single temperature tests, i.e. the constraint sensitivity tests, it appears that the R4PRZ displays a bimodal toughness distribution as seen in Fig. 3, while R3RPVH does not, as seen in Fig. 4. The rank probability is here

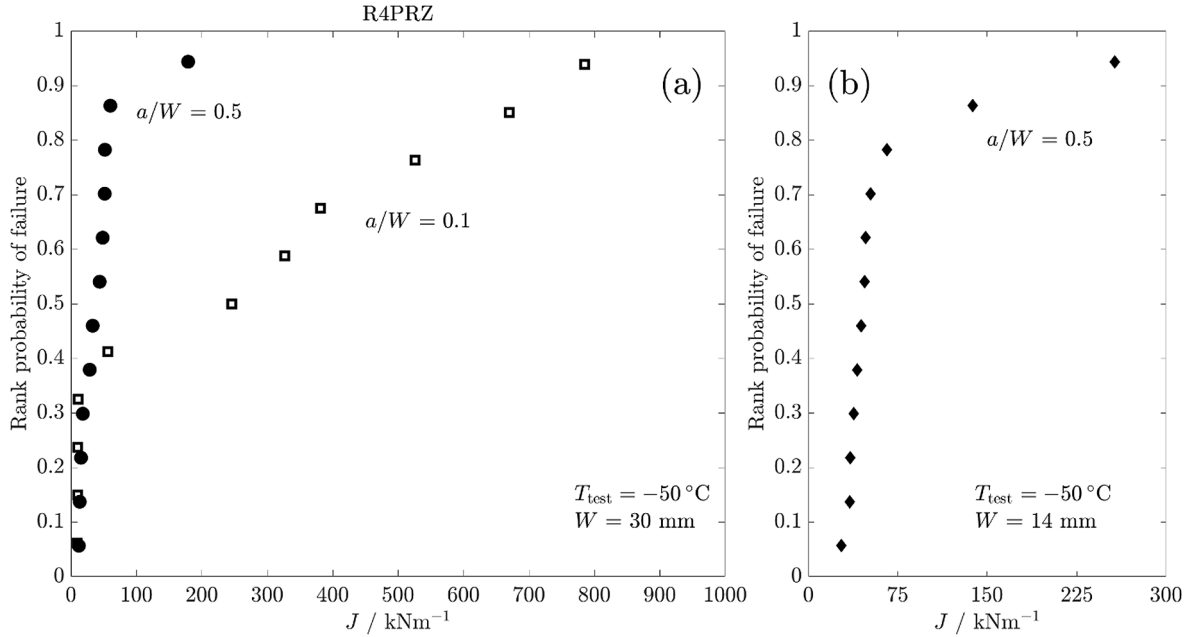


Fig. 3. Rank probabilities for the fracture tests of R4PRZ at the test temperature -50 °C. (a) Data sets where $W = 30$ mm and $a/W = \{0.5, 0.1\}$. (b) Data set where $W = 14$ mm and $a/W = 0.5$.

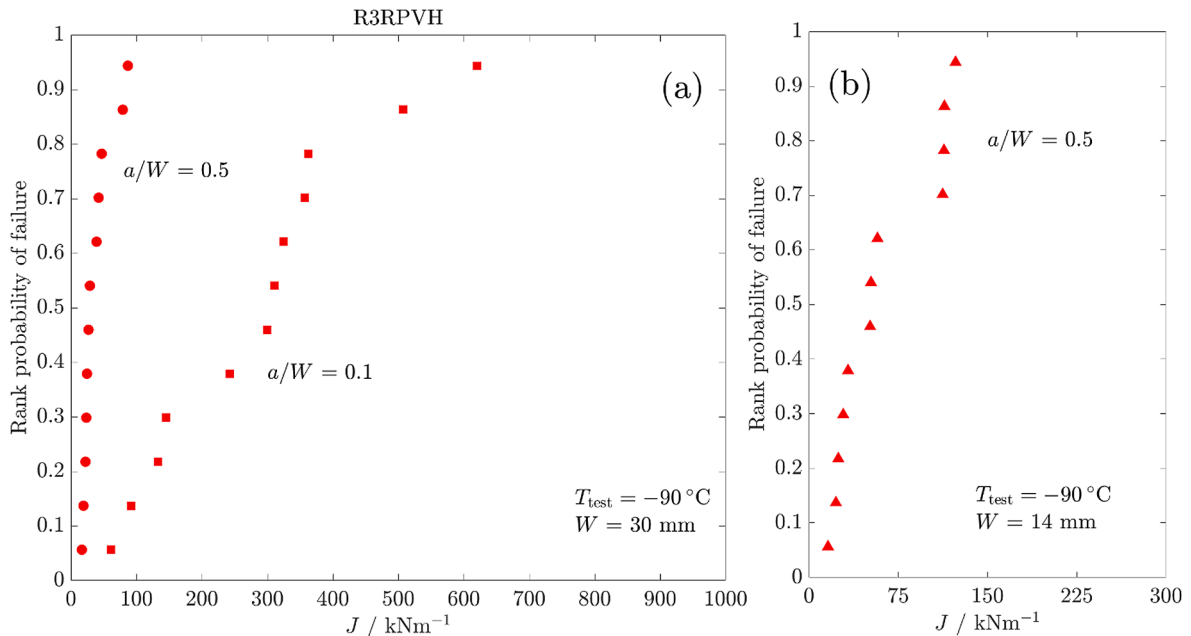


Fig. 4. Rank probabilities for the fracture tests of R3RPVH at the test temperature -90 °C. (a) Data sets where $W = 30$ mm and $a/W = \{0.5, 0.1\}$. (b) Data set where $W = 14$ mm and $a/W = 0.5$.

computed as the median rank by Benard's approximation $P_{rank}^i \approx (i - 0.3)/(N + 0.4)$.

Especially noticeable is that the low constraint R4PRZ specimens ($a/W=0.1$) behave very similar to the high constraint R4PRZ specimens ($a/W=0.5$) at rank probability levels below 0.4, where the fracture toughness essentially coincides (Fig. 3). While at higher levels of rank probability, the low constraint R4PRZ specimens ($a/W=0.1$) are subject to ductile crack growth up to 1 mm prior to brittle failure. Consequently, the scatter in fracture toughness, as expressed by the J -integral, becomes extreme and is found in the range 9.6 kN/m to 785 kN/m.

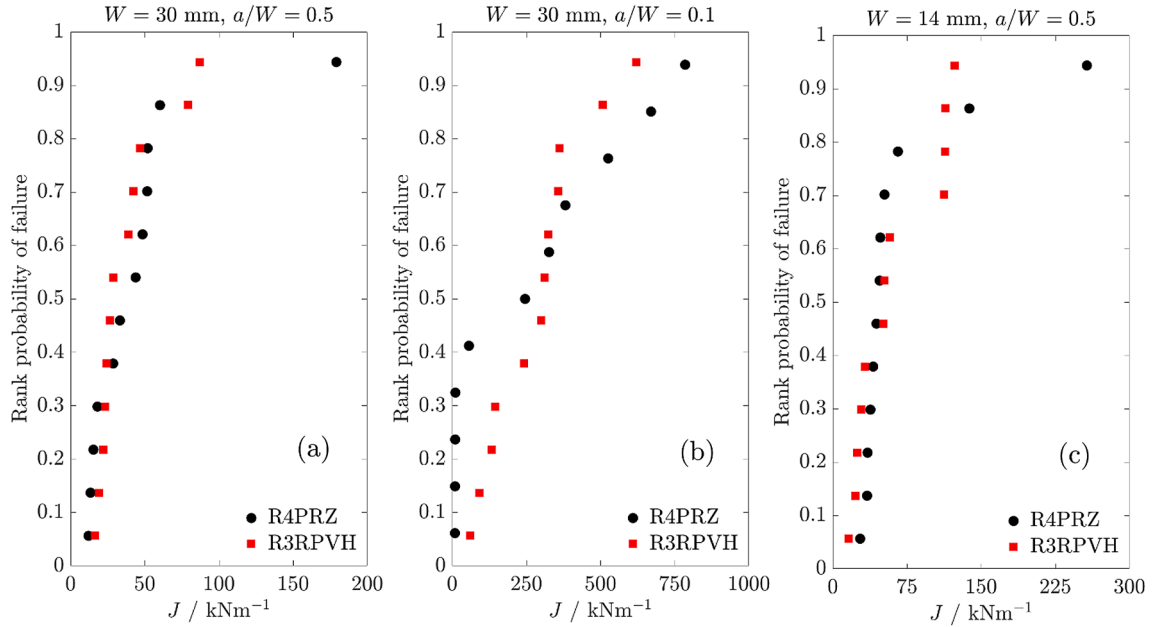


Fig. 5. Rank probabilities for the fracture tests of R4PRZ and R3RPVH for comparison of fracture toughness distribution. (a) Data set where $W = 30 \text{ mm}$ and $a/W = 0.5$. (b) Data set where $W = 30 \text{ mm}$ and $a/W = 0.1$. (c) Data set where $W = 14 \text{ mm}$ and $a/W = 0.5$.

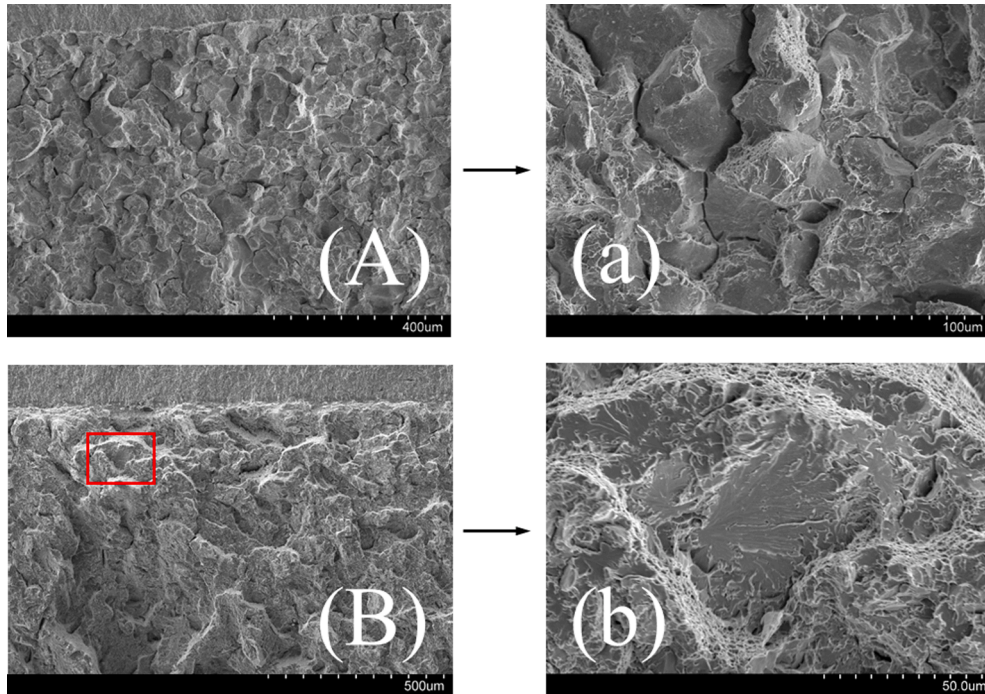


Fig. 6. Fractography of deeply cracked specimens ($a/W=0.5$) from the R4PRZ data set. Specimen {(A), (a)} fractured at a *low* toughness of $K_{IC} = 52 \text{ MPa}\sqrt{\text{m}}$, displays intergranular fracture, note secondary cracks in (a). Specimen {(B), (b)} fractured at a *higher* toughness of $K_{IC} = 108 \text{ MPa}\sqrt{\text{m}}$, displays transgranular fracture, probable initiation point in (b). The marked region in (B) shows where (b) is taken.

As seen in Fig. 5, the chosen temperatures for the constraint sensitivity tests were appropriate as the resulting fracture toughness distribution of the high constraint specimens (Fig. 5 a) shows a close similarity for both materials. In Fig. 5 (b), the low constraint results for both materials are compared, which clearly shows the difference between the thermally aged R4PRZ and the reference R3RPVH. In Fig. 5 (c), a comparison of the fracture toughness of the small specimens is shown, which aligns well, once again displaying the conformity of fracture toughness pertinent to high constraint geometries.

Fractography of the single temperature fracture tests presented in Fig. 3-Fig. 5 reveals that initiation of brittle fracture in the *low toughness specimens* from the thermally aged R4PRZ has occurred by grain boundary cracking. Here, the fracture surfaces are

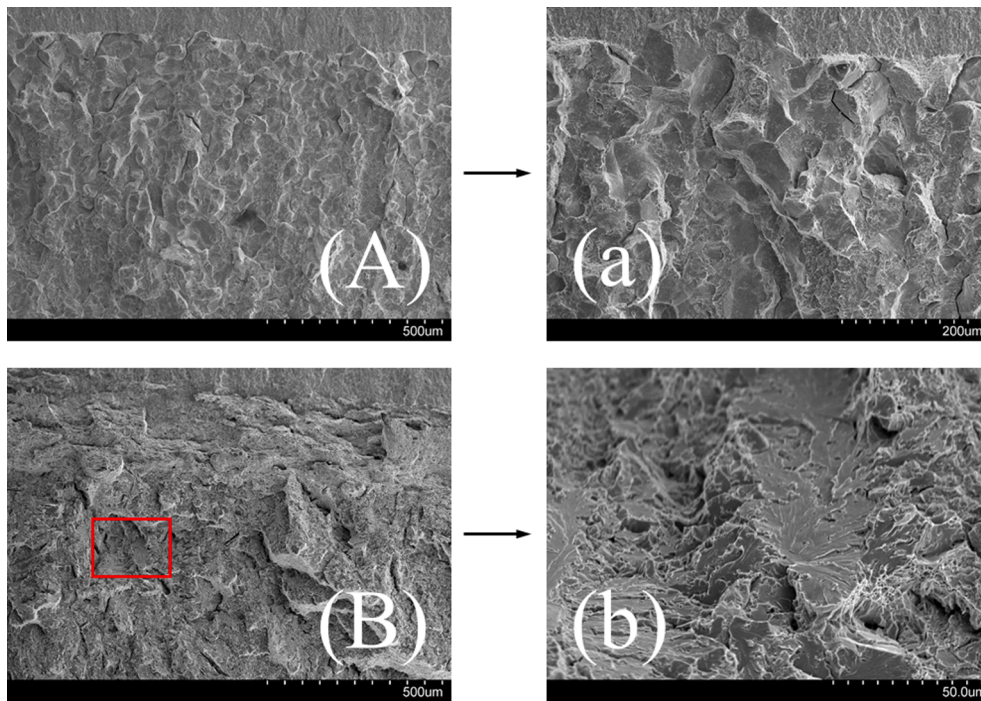


Fig. 7. Fractography of shallowly cracked specimens ($a/W = 0.1$) from the R4PRZ data set. Specimen {(A), (a)} fractured at a *low* toughness of $K_{JC} = 50 \text{ MPa}\sqrt{\text{m}}$, displays intergranular fracture, note secondary cracks in (a). Specimen {(B), (b)} fractured at a *higher* toughness of $K_{JC} = 270 \text{ MPa}\sqrt{\text{m}}$, displays transgranular fracture, probable initiation point in (b). The marked region in (B) shows where (b) is taken.

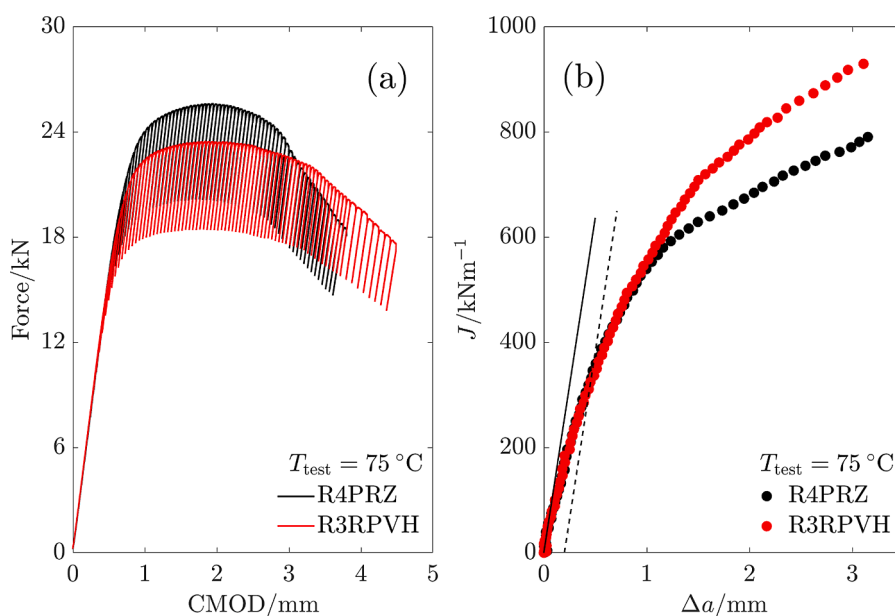


Fig. 8. Results from ductile fracture toughness testing. (a) Force-CMOD relation. (b) J - Δa relation.

consistently riddled with intergranular facets in direct connection to the crack front. This with no evidence of brittle fracture initiation from a second phase particle, as is commonly observed for cleavage fracture in ferritic steels. Observations of the *higher toughness specimens* unveil transgranular features and subsequently fracture initiation from second phase particles in tandem with intergranular features. For instance, low toughness brittle fracture appears to be solely associated with intergranular fracture while at higher levels of toughness, a mixture of both inter- and transgranular fracture appears to be the underlying cause of brittle fracture. Some examples of this is shown in Fig. 6 and Fig. 7 where low and high toughness specimens containing deep and shallow cracks are shown. For clarity, a low magnification image (uppercase) is associated with one of higher magnification (lowercase) per level of fracture toughness shown.

In the reference material R3RPVH, transgranular fracture is dominating the entire specimen population with few exceptions, where traces of intergranular fracture can be found in low toughness specimens. It should be noted that R3RPVH is not a perfect reference material, since it has been in operation during a significant number of years, however at a lower temperature and shorter time than R4PRZ.

The results from the ductile fracture toughness testing is shown in Fig. 8, where both the force-CMOD relation and the J_R -behavior for the two materials are shown. From these results it can be clearly distinguished that the ductile initiation fracture toughness $J_{IC} = 337 \text{ kN/m}$ is the same for both materials while the resistance to crack growth differs such that the thermally aged R4PRZ offers less resistance to crack growth after approximately 1 mm of growth.

3.2. Tensile and hardness tests

Fig. 9 shows a selection of the tensile tests that were carried out in this investigation. Fig. 9 (a) shows the tensile results at the testing temperatures pertinent to the constraint sensitivity fracture tests and it can be seen that the yield and ultimate tensile strength are virtually the same. Fig. 9 (b) displays the tensile results at room temperature, where it can be seen that the thermally aged R4PRZ appears to be slightly stronger than the reference R3RPVH. The tensile testing indicates that both materials are subjected to some hardening due to operation as the yield strength from the current investigation is higher than that of the check-in testing, a comparison is shown in Table 3.

The results from the Vickers hardness tests are shown in Fig. 10, where the hardness measured across and along the weld centerline in one of the R4PRZ and R3RPVH SEN(B)-specimens used for brittle fracture testing is plotted. It can clearly be seen that the hardness corresponds well with the results from the tensile tests in Fig. 9 for the two materials. For the hardness tests combined with heat treatments, annealing at 430 °C gave no change in hardness for times up to 50 h. However, annealing at 600 °C gave the results shown in

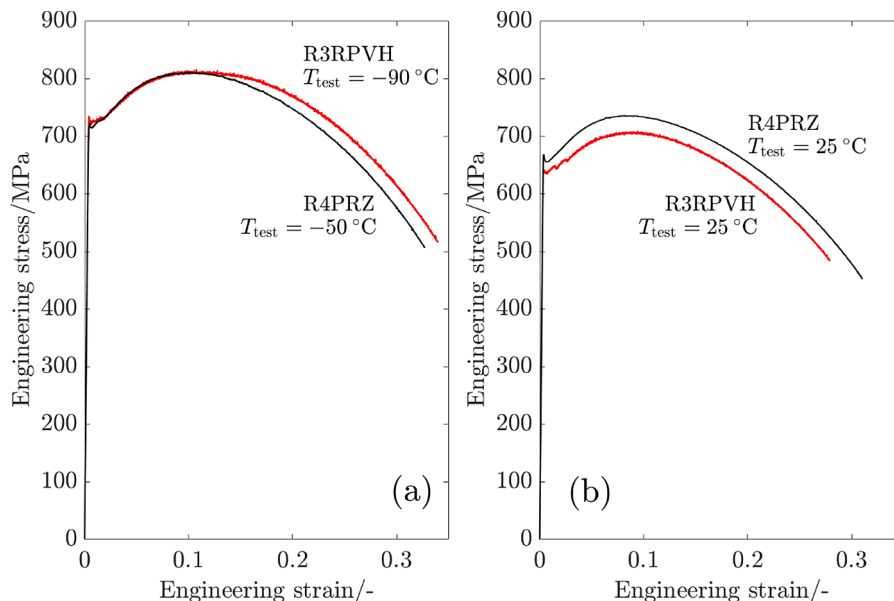


Fig. 9. Tensile tests of the weld metal of R4PRZ and R3RPVH. (a) At constraint sensitivity test temperatures. (b) At room temperature.

Table 3

Comparison between check-in yield strength and the results obtained in this investigation.

R_{p02}/MPa	Check-in	Current	Difference
R4PRZ	579	656	77
R3RPVH	575	637	62

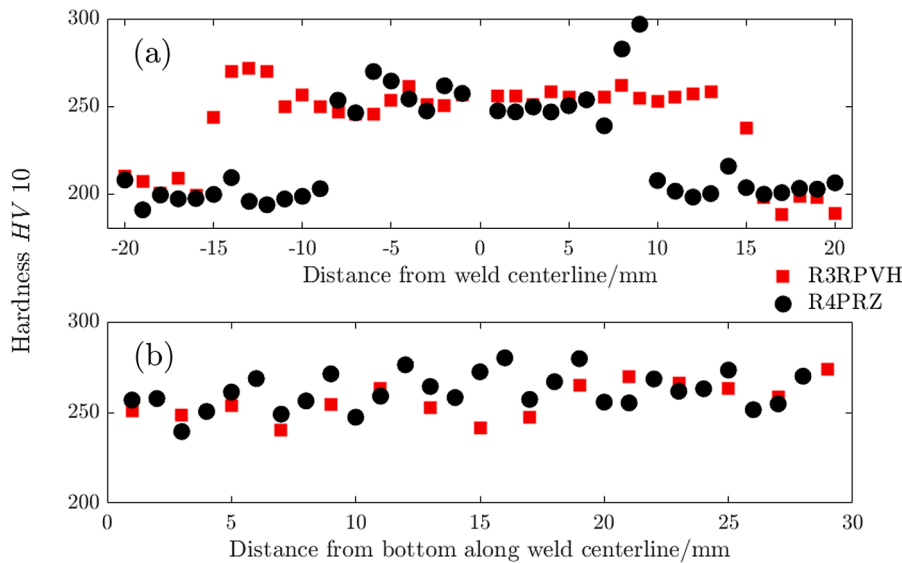


Fig. 10. Hardness measured on SEN(B)-specimens of R4PRZ and R3RPVH. (a) Shows the hardness across the weld centerline, from base metal to weld metal into base metal. (b) Shows the hardness along the weld centerline.

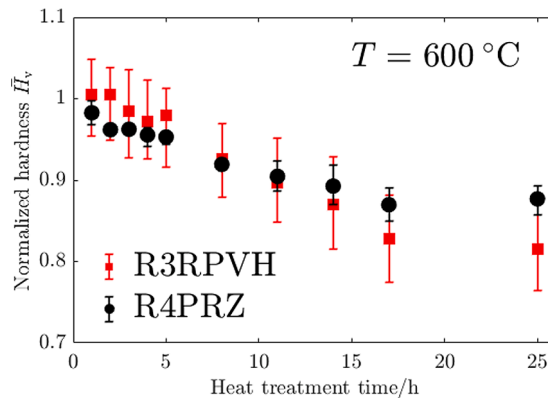


Fig. 11. Hardness of R4PRZ and R3RPVH against heat treatment time. Error bars represent the range in hardness measurement at each annealing.

Fig. 11, where normalized hardness is presented for both materials against annealing time. The error bars represent the range in hardness from the measurements after annealing. The initial hardness as defined by HV 10, of the specimens used in Fig. 11 can be represented by 248 and 254, which decreased to 220 and 213 after 25 h of annealing for R4PRZ and R3RPVH, respectively. It should be noted that a significant variability in hardness exists in the specimens, hence the wide range of the error bars.

3.3. Master curve analysis of single temperature fracture tests

By estimating the parameters of the bimodal master curve relevant to the single temperature fracture tests of R4PRZ, the results in Fig. 12 are obtained. When the three parameters are estimated for the high constraint specimen in Fig. 12 (a), it appears to give a consistent prediction of the size effect in Fig. 12 (c). However, there is no ambiguous way in which the bimodal master curve method can be constraint adjusted to reliably predict the experimental rank probabilities of the low constraint specimen in Fig. 12 (b). Therefore, the results presented in Fig. 12 (b) correspond to the low constraint specimen without corrections for loss of constraint. Furthermore, the bimodal master curve prediction in Fig. 12 (b) was based on a new set of parameters that were estimated to fit the experimental results shown in this graph. Thus, one set of bimodal parameters cannot be used to capture the experimental results of both the high and low constraint specimens displayed in Fig. 12. It should be noted that the master curve methodology, unimodal and bimodal, is based on self-similar crack tip fields related to a stationary crack, while the results in Fig. 12 (b) are subject to significant ductile crack growth prior to brittle failure. This will have an impact on the accuracy of the master curve with regards to parameter estimation and model predictions around and above the ductile initiation fracture toughness, $J_{IC} = 337 \text{ kN/m}$, $K_{JC} = 272 \text{ MPa } \sqrt{\text{m}}$.

In Fig. 13, master curve predictions of the probability of failure of the fracture tests of the reference material, R3RPVH are shown.

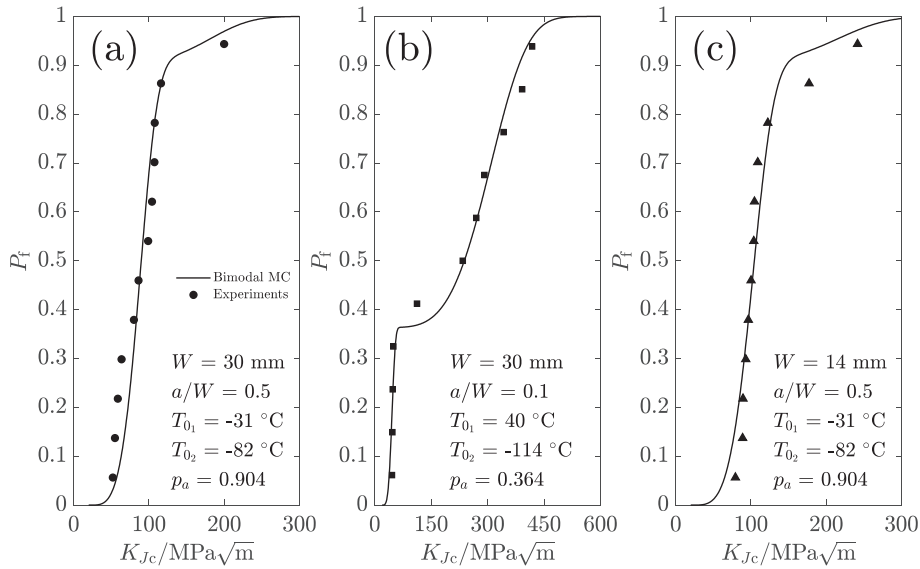


Fig. 12. Comparison of predicted failure probabilities (solid lines) from the bimodal master curve with rank probabilities for the experimental fracture tests pertaining to R4PRZ (symbols). (a) Data set where $W = 30 \text{ mm}$ and $a/W = 0.5$. (b) Data set where $W = 30 \text{ mm}$ and $a/W = 0.1$. (c) Data set where $W = 14 \text{ mm}$ and $a/W = 0.5$. Note, no constraint correction using e.g. T -stress has been used, the low constraint data has been used for both prediction and parameter estimation.

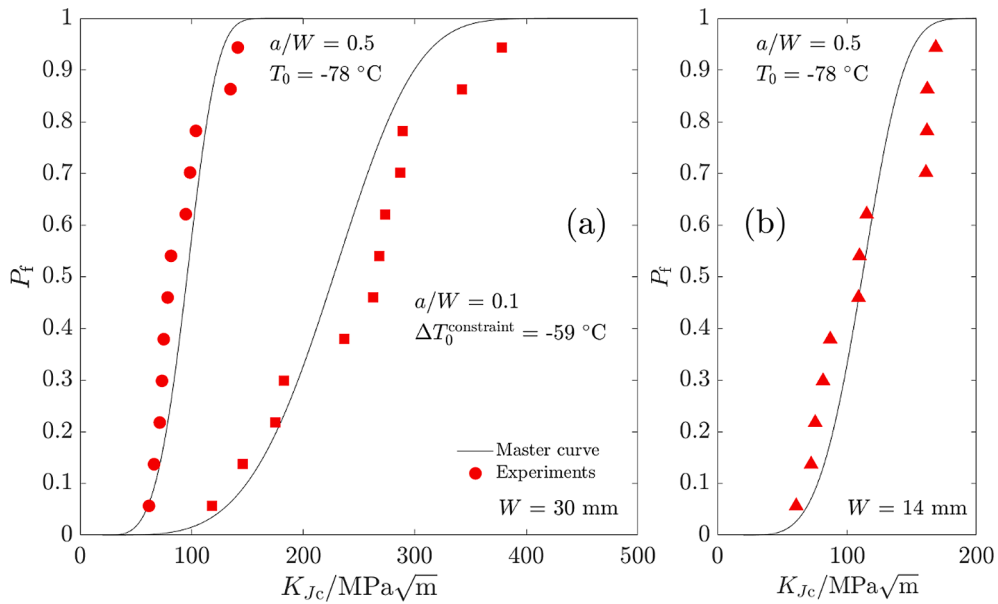


Fig. 13. Comparison of predicted failure probabilities (solid lines) from the (unimodal) master curve with rank probabilities for the experimental fracture tests pertaining to R3RPVH (symbols). (a) Data set where $W = 30 \text{ mm}$ and $a/W = 0.5$ and data set where $W = 30 \text{ mm}$ and $a/W = 0.1$. (b) Data set where $W = 14 \text{ mm}$ and $a/W = 0.5$. Note, T_0 has been subject to constraint correction using the T -stress for the low constraint specimens, $a/W = 0.1$ presented in (a).

Clearly, there is no need to use the bimodal master curve to describe the fracture toughness distribution of the reference material. The results presented in Fig. 13 (a) corresponding to the low constraint specimens ($a/W = 0.1$) are successfully constraint corrected using Eq. (4) where $A = \sigma_y/10 \text{ MPa/K}$.

3.4. Atom probe tomography

Regarding the results from the APT investigation, the measured chemical compositions of the matrix can be seen in Table 4. The

Table 4

Chemical matrix compositions as measured by APT. The standard deviation between different specimens is given as an estimate of the local variation in composition. N and S are omitted due to their overlaps with Si and O, respectively, in the APT spectrum.

At. %	R4PRZ	R3RPVH	Wt. %	R4PRZ	R3RPVH
C	0.03 ± 0.03	0.03 ± 0.01	C	0.01 ± 0.01	0.01 ± 0.01
Si	0.42 ± 0.09	0.47 ± 0.04	Si	0.21 ± 0.05	0.24 ± 0.02
P	0.02 ± 0.01	0.01 ± 0.01	P	0.01 ± 0.01	0.01 ± 0.01
V	0.004 ± 0.003	0.002 ± 0.001	V	0.004 ± 0.003	0.002 ± 0.001
Cr	0.13 ± 0.01	0.05 ± 0.01	Cr	0.12 ± 0.01	0.05 ± 0.01
Mn	1.33 ± 0.15	1.35 ± 0.07	Mn	1.31 ± 0.15	1.33 ± 0.07
Co	0.01 ± 0.01	0.02 ± 0.01	Co	0.01 ± 0.01	0.02 ± 0.01
Ni	1.69 ± 0.58	1.36 ± 0.08	Ni	1.78 ± 0.61	1.43 ± 0.08
Cu	0.05 ± 0.01	0.05 ± 0.01	Cu	0.06 ± 0.01	0.06 ± 0.01
Mo	0.12 ± 0.07	0.19 ± 0.07	Mo	0.21 ± 0.12	0.33 ± 0.12
Fe	Bal.	Bal.	Fe	Bal.	Bal.

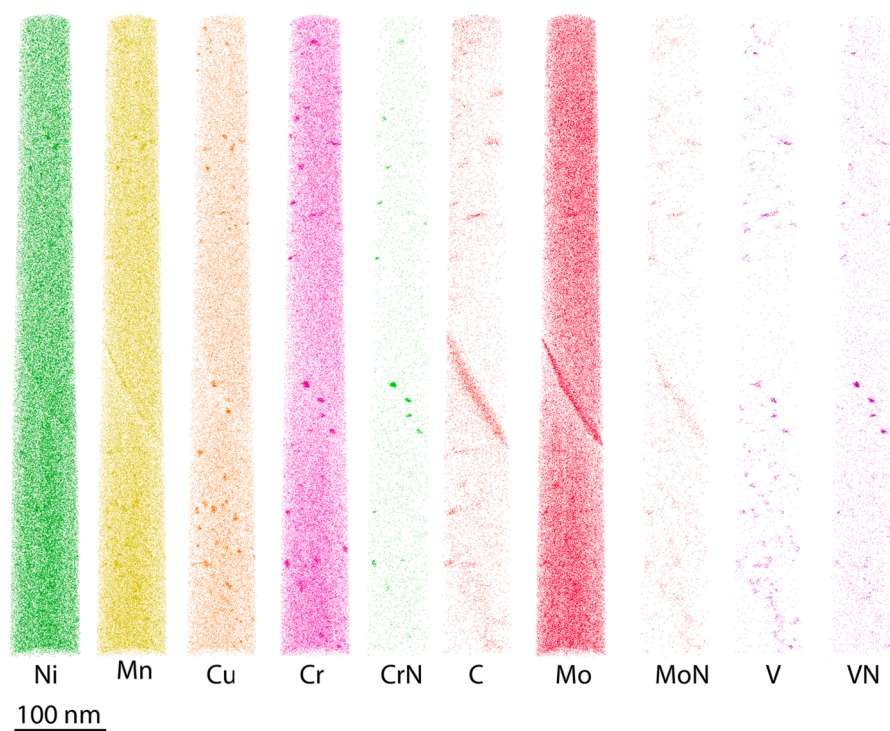


Fig. 14. APT reconstruction of thermally aged R4PRZ material. Only ions that are not randomly distributed are shown. This analysis was run in laser pulsed mode.

standard deviation between the different analyses of the same material is given, as APT is a local method and the welded material is chemically heterogeneous on the macroscopic scale. The average Ni content of the R4PRZ is slightly higher than that of R3RPVH. The average compositions are generally close to the nominal composition given in in Table 1. The low matrix concentration of C is expected as it is mainly present in carbides.

In the R4PRZ material, clusters were found using APT, see Fig. 14. The analyzed material was found to be heterogeneous; some of the smaller analyses did not contain any features whereas some contained many. Solute clusters containing Ni, Mn, Cu, and Si, were found in the reconstruction seen in Fig. 14. Some of these appear to have nucleated on very small carbonitrides. The carbonitrides contain V, Cr, Mo and some Mn, and some are found on dislocations, decorated with Mo, C, and Mn. As seen in the figure, not all carbonitrides contain all elements. The reconstruction in Fig. 14 also contain a boundary layer with Mo, C, some Ni, Si and Mn, and a few clusters/precipitates, out of which two appear to contain Cu and two do not.

A difficulty when analyzing the clusters and carbonitrides was the overlap in the mass spectrum at 32.5 Da. Both $^{65}\text{Cu}^{2+}$ and VN^{2+}

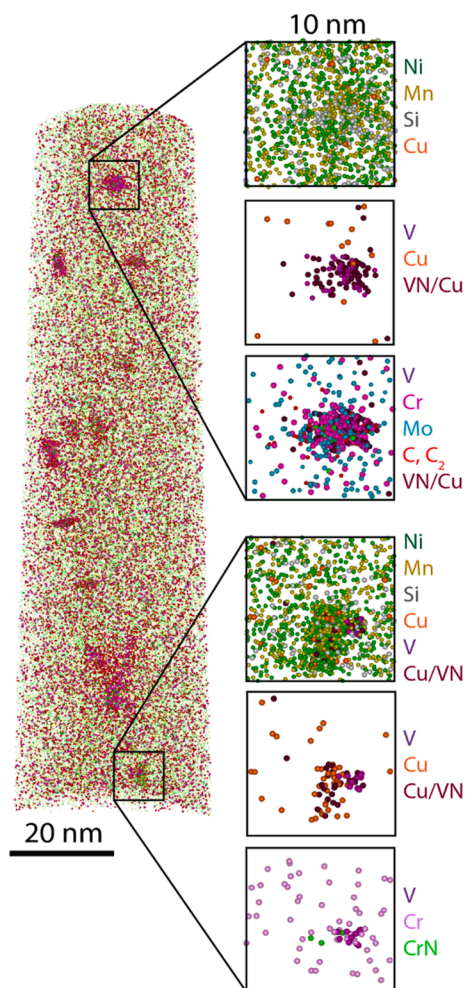


Fig. 15. Atom probe reconstruction of the thermally aged R4PRZ material. Two precipitates are cut out in boxes of $10 \times 10 \times 10 \text{ nm}^3$, with different elements shown. The upper V and Cr-rich carbonitride does not contain any Ni or Cu, and only small amounts of Mn. The ions marked VN/Cu are mainly VN. The lower precipitate contains mainly Ni, and Mn, and some Cu. There is also some V in one part of the precipitate. Most of the Cu/VN ions are probably Cu. This analysis was run in voltage pulsed mode.

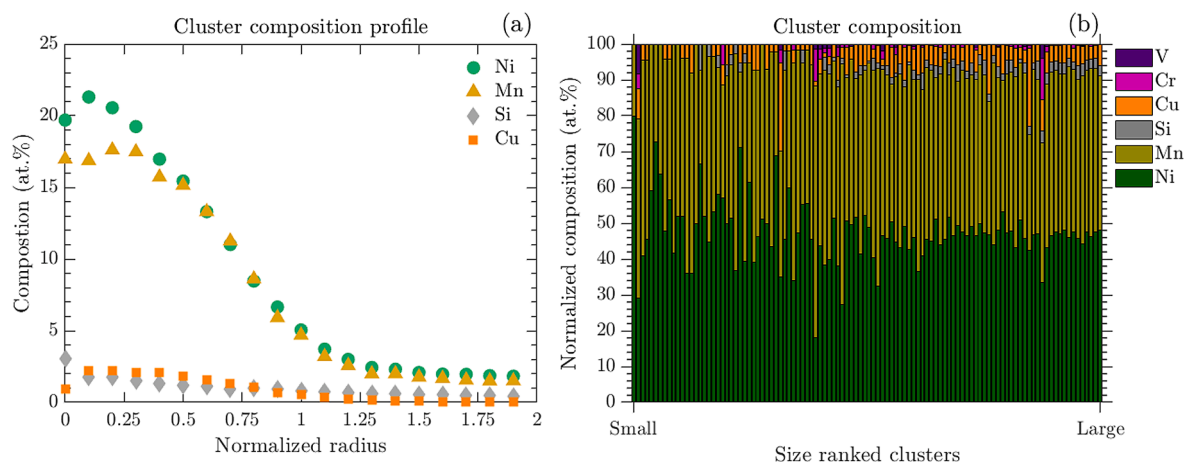


Fig. 16. The composition profile (a), and the cluster composition cluster by cluster (b), normalized by Fe in R4PRZ. The composition profile is not normalized in terms of composition, but the radius is. Zero corresponds to the cluster center, and unity to the edge of the cluster. The cluster composition cluster by cluster is sorted in increasing size.

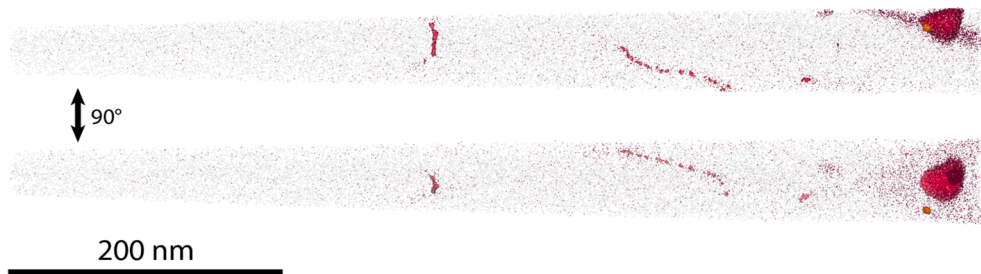


Fig. 17. APT reconstruction of the R3RPVH. Red iso-concentration surfaces correspond to Mo 1.9%, orange to Cu 1%, and brown dots are C atoms. A few dislocations are visible as well as a boundary layer containing a Mo-rich carbide and a small Cu-rich precipitate. The outline of the analysis is shown in grey. The reconstruction is turned 90°. (For interpretation of the references to colour in this figure legend, the reader is referred to the web version of this article.)

have peaks here in the voltage pulsed analyses. This was handled by using the peak at 31.5 Da to identify Cu^{2+} atoms, comparing with the local natural abundance of ^{65}Cu and ^{63}Cu . An example of this is shown in Fig. 15, where the upper precipitate is a carbonitride and the peak at 32.5 Da is mainly VN^{2+} . The 32.5 Da peak atoms then mainly coincide with the V atoms, whereas there are Cu atoms spread outside the carbonitride. In the lower cluster, that consists of mainly Ni, Mn, Si and Cu, the 32.5 Da peak is mainly $^{65}\text{Cu}^{2+}$, and the ions coincide with the $^{63}\text{Cu}^{2+}$ atoms at 31.5 Da. In laser pulsed runs the field is lower and thus most of the Cu evaporates as 1^+ ions [44]. In this case, the overlap problem is less prominent as VN still evaporates as VN^{2+} .

In Fig. 16, the normalized composition profile and the individual cluster compositions of one analysis are shown. The clusters contain mainly Ni and Mn, and smaller amounts of Cu and Si. It was found that the cluster Cu content varied between the different analyses, and that the example in Fig. 16 is low in Cu. The clusters have similar composition within the same analysis. Many of the clusters contain some V or Cr. The average diameter of the Ni-Mn-rich clusters was also varying between the analyses, but the average was found to be 2.1 ± 0.3 nm, and the number density $1.3 \pm 0.5 \cdot 10^{22} / \text{m}^3$.

The reference material from the RPVH of Ringhals R3, R3RPVH, was also analysed using APT. One reconstruction can be found in Fig. 17. In general, this material contained a lower density of small carbonitrides than the pressurizer. Still, some were found, and also Mo and C enriched dislocations, and boundaries. In Fig. 17 a Mo-rich carbide is sitting on a boundary.

Interestingly, occasional clusters containing Cu, Ni, and Mn were found in the R3RPVH material. In Fig. 17, one is present on the boundary layer. In other reconstructions, a few clusters were found on dislocations. The number density of the precipitates was very low, and they were not homogeneously distributed.

4. Discussion

The in-service thermal ageing of the pressurizer weld metal from Ringhals unit 4 appears to manifest through both hardening and non-hardening embrittlement mechanisms. That is, both by an increase in yield strength and by a weakening of the grain boundaries of the material. The effects of the embrittlement due to thermal ageing are profound in that they both give a significant change in the reference temperature T_0 and affects the fracture toughness distribution. As seen in Figs. 3-5 the comparison between the fracture toughness distributions of R4PRZ and R3RPVH reveals that there are some apparent differences at conditions that should be equal in terms of the high constraint fracture toughness. The most notable difference being that the low constraint specimens of R4PRZ shows a very wide range in the test data, where the most brittle specimens display fracture initiation through intergranular fracture and the tougher specimens appear to experience brittle fracture initiation from both grain boundaries and second phase particles, where the latter appears to bring out transgranular fracture features.

The toughness distribution of the R4PRZ appears to be bimodal where the bimodality has its origin in the multiple initiation mechanisms. This indicates that failure initiated from a grain boundary is weaker than that of failure initiated from a second phase particle in this material. The upper part of the distribution for the R4PRZ appears to be tougher than that of R3RPVH, which is likely an effect of ductile crack growth that occurs prior to the final brittle fracture. It is also important to note that the ductile crack growth that occurs prior to the final brittle failure will further pronounce the bimodality of the fracture toughness distribution. However, it is of the opinion of the authors that ductile crack growth alone cannot produce the effect that is seen in the fracture toughness results of the aged material. Clearly, it is the effect of multiple mechanisms acting to initiate brittle fracture that causes the bimodal fracture toughness distribution that acts concurrently with a ductile crack growth process.

For describing the toughness distribution of the thermally aged R4PRZ, the bimodal master curve is required and appears to be able to describe the material well under conditions of high constraint. The reference material R3RPVH is well described by the standard master curve, i.e. the *unimodal* model. However, the transition between the high and low constraint geometries is not trivial. For the case of R3RPVH, the correction of T_0 for the low constraint $a/W = 0.1$ appears to work well using Wallin's empirical relation [32]. But, a constraint correction for the bimodal master curve that ideally should be used to describe the R4PRZ is currently ambiguous due to the complex interactions of the initiation mechanisms and the number of parameters included in the model. A weakest link model capable of describing two brittle initiation mechanisms as well as predicting the size and constraint effect in a satisfactory manner has been proposed in Boåsen et al. [45].

Separating the effects from hardening and non-hardening contributions to the change in fracture toughness is not straight-forward. From the fractography of the thermally aged R4PRZ, the effects of non-hardening embrittlement can be distinguished from the presence of intergranular features. The hardening contribution was elucidated by the combination of hardness tests and heat treatments. From the measurements presented in Fig. 11, the hardness in both materials can be seen to decrease by 12–18 %, which is similar to the difference between the yield strengths obtained in the current investigation and the check-in data. It should also be noted that the decrease in hardness is to a level judged to be relevant to the as-manufactured hardness of the weld. This implies that there is a hardening effect present in both the R4PRZ and the R3RPVH materials, i.e. hardening due to thermal ageing at the operating temperatures.

Concerning the ductile fracture tests presented in Fig. 8, the fracture toughness plotted against crack growth aligns well for crack growth up to ~ 1 mm, thereafter it deviates so that the R4PRZ has less resistance than R3RPVH. This is accompanied with a change in fracture surface appearance where the morphology changes notably. A possible explanation would be that the crack grows into a different part of the microstructure, which presents different requisites for void growth and coalescence, the main operating mechanism for ductile crack growth in these materials. As an example, if the crack starts growing in a zone with a reheated microstructure (small equiaxed grains), it is likely that the ductile fracture resistance will change once the crack grows into an as-welded zone (elongated dendritic grains), or vice versa.

The obvious material to compare the APT-results of the R4PRZ material with is the pressurizer weld analysed by APT in [21] and [46]. This weld comes from the very same component, but a different weld that is slightly different in terms of composition. The clusters containing Cu, Ni, Mn, and Si are relatively similar in appearance. The Cu content is higher in the clusters reported in [21] and [46], but the measured Cu content is also higher in that weld (0.10 at. % compared to the 0.05 at. % in the weld in this paper). The lower Cu content makes the core-shell structure (Cu-rich core) less prominent in the clusters here. The cluster size and number density of the two studies of pressurizer welds are within the estimated errors considering the heterogeneous distribution.

As mentioned earlier, the terms cluster and precipitate are used interchangeably in this paper, as APT does not provide enough crystallographic information to reveal the crystal structure of these small clusters/precipitates. Generally, bcc Cu-clusters in α -Fe are believed to transform into 9R precipitates when they have a diameter of at least around 4 nm, and into fcc at larger sizes [47,48]. Here, the Ni and Mn content of the clusters is high, and thus the question is what type of precipitate is formed, and at which diameter.

The most significant difference from the other weld of the same pressurizer is the amount of small carbonitrides. In the other material, occasional V and Cr-containing carbonitrides were found. They were also found in the reference material used in that paper and in the Ringhals RPV weld metal [20]. It is assumed that the carbonitrides are present before ageing and are thus not affecting the shift of mechanical properties in a direct way. They appear to act as nucleation point for the Ni-Mn-rich clusters, as many of them are found in connection to each other (see Figs. 14–16). The higher number of carbonitrides does, however, not seem to give a significant increase in the number of Ni-Mn-Cu-Si clusters as the number density of $1.3 \cdot 10^{22} / \text{m}^3$ here is close and within the uncertainty of the $1.6 \cdot 10^{22} / \text{m}^3$ measured in [21]. Also, there are carbonitrides where Cu, Ni, Mn and Si have not precipitated/clustered, see Figs. 14 and 15.

The fact that Ni-Mn-Cu-Si clusters could be found in the R3RPVH material that was used as reference material is interesting. Such clusters were not found in similar un-aged reference materials used by the authors in similar high Ni and Mn, low Cu weld metals [21,20]. Despite the diffusion of these elements in α -Fe being very slow at the relevant temperature (310–315 °C), some clustering still seems to be possible, although to a very limited degree.

5. Conclusions

The effects of embrittlement due to thermal ageing on the weldments from a pressurizer of a Swedish nuclear power plant, more specifically the effect of ageing on the constraint sensitivity of the fracture toughness has been investigated and compared to a reference material. Testing revealed a $\Delta T_0 = 45$ °C between the materials, indicating a significant embrittlement. The thermally aged material displays a bimodal fracture toughness distribution, which is pronounced at low constraint, and is due to brittle fracture being initiated from weakened grain boundaries as well as second phase particles. To describe the fracture toughness distribution, the bimodal master curve is needed and no constraint correction for the low constraint specimens can unambiguously be made. The reference material is well described by the unimodal master curve and the constraint effect is well predicted within the same framework.

The nanostructure of both materials is characterized using atom probe tomography. In-homogeneously distributed solute clusters of Ni-Mn-Cu-Si situated on dislocations and on carbonitrides, which are also present within the material, were observed.

A hardening due to thermal ageing is apparent in both the studied materials. It is investigated using uniaxial tensile tests as well as hardness tests in combination with heat treatments. After annealing at 600 °C for 25 h it appears that the ageing induced hardening is restored, most likely due to dissolution of solute clusters formed due to thermal ageing.

CRedit authorship contribution statement

Magnus Boåsen: Conceptualization, Data curation, Formal analysis, Investigation, Methodology, Project administration, Software, Visualization, Validation, Writing – original draft, Writing – review & editing. **Kristina Lindgren:** Conceptualization, Formal analysis, Investigation, Methodology, Software, Visualization, Writing – original draft, Writing – review & editing. **Martin Öberg:** Methodology, Resources, Software, Supervision, Writing – review & editing. **Mattias Thuvander:** Conceptualization, Methodology, Resources, Supervision, Writing – original draft, Writing – review & editing, Funding acquisition. **Jonas Faleskog:** Conceptualization, Investigation, Methodology, Supervision, Writing – original draft, Writing – review & editing. **Pål Efsing:** Conceptualization, Funding

acquisition, Investigation, Methodology, Project administration, Resources, Supervision, Writing – original draft, Writing – review & editing.

Declaration of Competing Interest

The authors declare that they have no known competing financial interests or personal relationships that could have appeared to influence the work reported in this paper.

Acknowledgements

The Swedish Radiation Safety Authority (SSM) and the Swedish Centre for Nuclear Technology (SKC) are acknowledged for their financial support. Ringhals AB is acknowledged for supplying the material that was used in the experimental investigation. Jenny Roudén at Ringhals AB is greatly acknowledged for her support in this study and for constructive comments on the manuscript. The APT was performed at the Chalmers Materials Analysis Laboratory (CMAL).

References

- [1] Debarberis L, Acosta B, Zeman A, Pirfo S, Moretto P, Chernobaeva A, et al. Ductile-to-brittle transition temperature of thermally segregated WWER-1000 base metal. *Int J Microstruct Mater Prop* 2007;2(3/4):326. <https://doi.org/10.1504/IJMMP.2007.015312>.
- [2] Gurovich BA, Chernobaeva AA, Yu Erak D, Kuleshova EA, Zhurko DA, Papina VB, et al. Chemical composition effect on VVER-1000 RPV weld metal thermal ageing. *J Nucl Mater* 2015;465:540–9.
- [3] A. A. Chernobaeva, E. A. Kuleshova, B. A. Gurovich, D. Yu Erak, O. O. Zabusov, D. A. Maltsev, D. A. Zhurko, V. B. Papina and M. A. Skundin, "Thermal ageing effects of VVER-1000 weld metal under operation temperature," in *Fontevraud 8*, Avignon, 2014.
- [4] Shtrombakh YI, Gurovich BA, Kuleshova EA, Maltsev DA, Fedotova SV, Chernobaeva AA. Thermal ageing mechanisms of VVER-1000 reactor pressure vessel steels. *J Nucl Mater* 2014;452(1-3):348–58.
- [5] Joly P, Roch F, Primault C. Effect of thermal ageing on properties of pressure vessel low alloy steel. *Proceedings of the ASME 2013 Pressure Vessels and Piping Conference*. 2013.
- [6] Pelli R, Forstén J. Effect of thermal ageing on impact ductility of the nuclear pressure vessel steel SA533B and its weld metal. *Theor Appl Fract Mech* 1987;8: 25–31.
- [7] Kameda J, Nishiyama Y. Combined effects of phosphorus segregation and partial intergranular fracture on the ductile-brittle transition temperature in structural alloy steels. *Mater Sci Engng, A* 2001;528:3705–13.
- [8] Andrieu A, Pineau A, Joly P, Roch F, Ryckelynck D. Influence of P and C intergranular segregation during manufacturing and ageing on the fracture toughness of nuclear pressure vessel steels. *Procedia Mater Sci* 2014;3:655–60.
- [9] S. G. Druce, G. Gage and J. G., "Effect of ageing on properties of pressure vessel steels," *Acta Metallurgica*, vol. 34, no. 4, pp. 641–652, 1986.
- [10] Vatter IA, Hipsley CA, Druce SG. Review of Thermal Ageing Data and its Application to Operating Reactor Pressure Vessels. *Int J Press Vessels Pip* 1993;54(1-2):31–48.
- [11] Naudin C, Frund JM, Pineau A. Intergranular fracture stress and phosphorus grain boundary segregation of a Mn-Ni-Mo steel. *Scr Mater* 1999;40(9):1013–9.
- [12] Briant CL, Banerji SK. Intergranular failure in steel: the role of grain boundary composition. *Int Metal Rev* 1978;23(1):164–99.
- [13] McMahon CJ. Intergranular Fracture in Steels. *Mater Sci Eng* 1976;25:233–9.
- [14] Guttman M. Equilibrium segregation in a ternary solution: a model for temper embrittlement. *Surf Sci* 1975;53(1):213–27.
- [15] Guttman M. Temper Embrittlement and Ternary Equilibrium Segregation. *Mater Sci Eng* 1980;42:227–32.
- [16] Banerji SK, McMahon CJ, Feng HC. Intergranular Fracture in 4340-Type Steels: Effects of Impurities and Hydrogen. *Metall Trans A* 1978;9(2):237–47.
- [17] Stein DF. Reversible temper embrittlement. *Annu Rev Mater Res* 1977;7(1):123–53.
- [18] Miller MK, Powers KA, Nanstad RK, Efsing P. Atom probe tomography characterizations of high nickel, low copper surveillance RPV welds irradiated to high fluences. *J Nucl Mater* 2013;437(1-3):107–15.
- [19] Styman PD, Hyde JM, Parfitt D, Wilford K, Burke MG, English CA, et al. Post-irradiation annealing of Ni-Mn-Si-enriched clusters in a neutron-irradiated RPV steel weld using Atom Probe Tomography. *J Nucl Mater* 2015;459:127–34.
- [20] Lindgren K, Boåsen M, Stiller K, Efsing P, Thuvander M. Evolution of precipitation in reactor pressure vessel steel welds under neutron irradiation. *J Nucl Mater* 2017;488:222–30.
- [21] Lindgren K, Boåsen M, Stiller K, Efsing P, Thuvander M. Cluster formation in in-service thermally aged pressurizer welds. *J Nucl Mater* 2018;504:23–8.
- [22] Hyde JM, Sha G, Marquis EA, Morley A, Wilford KB, Williams TJ. A comparison of the structure of solute clusters formed during thermal ageing and irradiation. *Ultramicroscopy* 2011;111(6):664–71.
- [23] Styman PD, Hyde JM, Wilford K, Morley A, Smith GDW. Precipitation in long term thermally aged high copper, high nickel model RPV steel welds. *Prog Nucl Energy* 2012;57:86–92.
- [24] Styman PD, Hyde JM, Wilford K, Smith GDW. Quantitative methods for the APT analysis of thermally aged RPV steels. *Ultramicroscopy* 2013;132:258–64.
- [25] Styman PD, Hyde JM, Wilford K, Parfitt D, Riddle N, Smith GDW. Characterisation of interfacial segregation to Cu-enriched precipitates in two thermally aged reactor pressure vessel welds. *Ultramicroscopy* 2015;159:292–8.
- [26] Viehriq H-W, Houska M, Kalkhof D, Schindler H-J. Fracture mechanics characterisation of reactor pressure vessel multi-layer weld metal. *Int J Press Vessels Pip* 2015;135-136:36–51.
- [27] ASTM International, "E1921 Standard Test Method for Determination of Reference Temperature, T₀, for Ferritic Steels in the Transition Range," ASTM International, West Conshohocken, 2019.
- [28] Faleskog J, Kroon M, Öberg H. A probabilistic model for cleavage fracture with a length scale - parameter estimation and predictions of stationary crack experiments. *Engng Fract Mech* 2004;71(1):57–79.
- [29] Wallin K. The scatter in KIC-results. *Engng Fract Mech* 1984;19(6):1085–93.
- [30] Pisarski HG, Wallin K. The SINTAP fracture toughness estimation procedure. *Engng Fract Mech* 2000;67(6):613–24.
- [31] Wallin K, Nevasmaa P, Laukkanen A, Planman T. Master Curve analysis of inhomogeneous ferritic steels. *Engng Fract Mech* 2004;71:2329–46.
- [32] Wallin K. Quantifying T-stress controlled constraint by the master curve transition temperature T₀. *Engng Fract Mech* 2001;68:303–28.
- [33] Wallin K. *Fracture Toughness of Engineering Materials - Estimation and Application*. Croydon: EMAS Publishing; 2011.
- [34] Boåsen M, Stec M, Efsing P, Faleskog J. A generalized probabilistic model for cleavage fracture with a length scale - Influence of stress state and application to surface cracked experiments. *Engng Fract Mech* 2019;214:590–608.
- [35] ASTM International, "E1820 Standard Test Method for Measurement of Fracture Toughness," ASTM International, West Conshohocken, 2019.
- [36] Hyde JM, Burke MG, Gault B, Saxey DW, Styman P, Wilford KB, et al. Atom probe tomography of reactor pressure vessel steels: an analysis of data integrity. *Ultramicroscopy* 2011;111(6):676–82.
- [37] Miller MK. *Atom Probe Tomography: Analysis at the Atomic Level*. Academic/Plenum Publishers 2000;200.

- [38] Hyde JM, English CA. "An Analysis of the Structure of Irradiation induced Cu-enriched Clusters in Low and High Nickel Welds," in *Materials Research Society Symposium*. Boston 2000;650. <https://doi.org/10.1557/PROC-650-R6.6>.
- [39] Vaumousse D, Cerezo A, Warren PJ. A procedure for quantification of precipitate microstructures from three-dimensional atom probe data. *Ultramicroscopy* 2003;95:215–21.
- [40] Dong Y, Etienne A, Frolov A, Fedotova S, Fujii K, Fukuya K, et al. Atom Probe Tomography Interlaboratory Study on Clustering Analysis in Experimental Data Using the Maximum Separation Distance Approach. *Microsc Microanal* 2019;25(2):356–66.
- [41] Lindgren K, Stiller K, Efsing P, Thuvander M. On the Analysis of Clustering in an Irradiated Low Alloy Reactor Pressure Vessel Steel Weld. *Microsc Microanal* 2017;23(2):376–84.
- [42] Marquis EA, Hyde JM. Applications of atom-probe tomography to the characterization of solute behaviours. *Mater Sci Eng R Rep* 2010;69(4–5):37–62.
- [43] Edmondson PD, Parish CM, Nanstad RK. Using complimentary microscopy methods to examine Ni-Mn-Si-precipitates in highly-irradiated reactor pressure vessel steels. *Acta Mater* 2017;134:31–9.
- [44] Kingham DR. The Post-Ionization of Field Evaporated Ions: a Theoretical explanation of Multiple Charged States. *Surf Sci* 1982;116:273–301.
- [45] Boåsen M, Dahlberg CFO, Efsing P, Faleskog J. A weakest link model for multiple mechanism brittle fracture - Model development and application. *J Mech Phys Solids* 2021;147:104224.
- [46] K. Lindgren, M. Boåsen, K. Stiller, P. Efsing and M. Thuvander, "Thermal ageing of low alloy steel weldments from a Swedish nuclear power plant - the evolution of the microstructure," in *Fontevraud 9*, Avignon, 2018.
- [47] Deschamps A, Militzer M, Poole WJ. Comparison of Precipitation Kinetics and Strengthening in an Fe-0.8%Cu Alloy and a 0.8% Cu-containing Low-carbon Steel. *ISIJ Int* 2003;43:1826–32.
- [48] Othen PJ, Jenkins ML, Smith GDW. High-resolution electron microscopy studies of the structure of Cu precipitates in α -Fe. *Philos Mag A* 1994;70: 1–24.